



Fracture mechanisms in Ti and Co–Cr growing rods and impact on clinical practice[☆]

Arnaud Ribesse^a, Karim Ismail^a, Maïté Croonenborghs^a, Nadia Irda^b, Lotfi Miladi^c, Pascal J. Jacques^a, Maryline Mousny^d, Thomas Pardoën^{a,*}

^a Institute of Mechanics, Materials and Civil Engineering, UCLouvain, Place Sainte Barbe 2 L5.02.02, 1348, Louvain-la-Neuve, Belgium

^b Department of Orthopedics, Cliniques Universitaires Saint-Luc, Avenue Hippocrate 10, 1200, Bruxelles, Belgium

^c Hôpital Necker, Service d'Orthopédie, 149 Rue de Sèvres, 75 015, Paris, France

^d Centre Plurisanté, 11 avenue de l'Andalousie, 1140, Bruxelles, Belgium

ARTICLE INFO

Keywords:

Early onset scoliosis
Growing rod
Single-rod construct
Rod fracture
Fracture surface analysis
Fatigue cracking
Analytical model

ABSTRACT

The widely used treatment of early onset scoliosis based on fusionless spinal instrumentation with growing rods suffers from severe complications due to premature rod failure. Only few studies have explored the fracture mechanisms in single rod constructs, while clinical practice urgently needs guidance. The objectives of this study are (i) to determine the failure mechanisms in Ti–6Al–4V alloy, Ti Cp 2 and Co–Cr alloy rods, and (ii) to propose strategies to reduce the risk of rod fracture. For this purpose, seven rods from three patients treated for early onset scoliosis were characterized by preoperative, pre-fracture X-rays and after-fracture X-rays. Fracture surface analysis, performed using scanning electron microscopy, revealed similar failure mechanisms for all rods, independent of composition and diameter. Fracture is caused by fatigue, associated to repeated bending action in the anteroposterior direction. Cracking initiates at multiple sites. Three-point bending fatigue tests on Ti–6Al–4V bent rods confirmed the fracture scenario. A beam bending model indicates that the failure process is controlled by the combination of cyclic vertical and horizontal forces with amplitudes from 200 N to 400 N and from 70 N to 150 N, respectively. Strategies to minimize fracture involve adaptations of material properties and rod geometry to scoliosis characteristics, including sagittal alignment, and spine behavior.

1. Introduction

The management of progressive early onset scoliosis (EOS) is a challenging medical issue. The treatment should produce and maintain a correction without interfering with the spinal growth and lung development (Akbarnia and Emans, 2010). A surgical treatment is considered in case of brace/cast treatment failure or of contraindication (Patterson et al., 1990; Thompson et al., 2007). Growth-friendly techniques were progressively developed and nonfusion procedures (growing rod based techniques) are now commonly used for the management of evolutive EOS, unresponsive to conservative treatment (Akbarnia et al., 2005; Hickey et al., 2014; Thompson et al., 2007; Yazici and Olgun, 2013).

Fusionless surgeries exhibit high complication rates, whatever treatment modality, as reported by (Akbarnia and Emans, 2010; Bess

et al., 2010; Sankar et al., 2010; Watanabe et al., 2013). Fig. 1 shows an example of a growing rod fracture through a comparison of X-rays at the time of insertion and after fracture. The consequences of a growth-rod failure are quite dramatic. They lead to severe pain, to a loss of the scoliosis correction and to the need for a new invasive surgery. Such failure events have been described by different authors (e.g. Bess et al., 2010; Yang et al., 2011), but the underlying failure mechanisms are still poorly understood. Yang et al. studied 86 stainless steel or titanium alloy broken rods from both single-rod and dual-rod constructs in 49 patients and determined the fracture location based on X-ray images (Yang et al., 2011). The most common fracture locations were above or below the tandem connectors (34 out of 86) and near the thoracolumbar junction (35 out of 86). Standard dual growing rods, hybrid growing rods with rib anchors proximally and spine anchors distally, and vertical expandable

[☆] This work is submitted as a Research Paper.

* Corresponding author.

E-mail addresses: arnaud.ribesse@hotmail.com (A. Ribesse), karim.ismail70@gmail.com (K. Ismail), maite.croonenborghs@uclouvain.be (M. Croonenborghs), nadia.irda@uclouvain.be (N. Irda), l.miladi@aphp.fr (L. Miladi), pascal.jacques@uclouvain.be (P.J. Jacques), maryline.mousny@gmail.com (M. Mousny), thomas.pardoen@uclouvain.be (T. Pardoën).

<https://doi.org/10.1016/j.jmbbm.2021.104620>

Received 29 December 2020; Received in revised form 15 April 2021; Accepted 28 May 2021

Available online 2 June 2021

1751-6161/© 2021 Elsevier Ltd. All rights reserved.

prosthetic titanium rib are the most commonly used techniques. Single growing rod techniques exhibit a higher complication rate compared to dual-rod constructs (Akgül et al., 2014). Regarding the failure of dual-rod constructs, Yamanaka et al. observed fatigue crack patterns and suggested that these fatigue cracks occurred during rod use, whereas the application of a large external stress, during falling or twisting movements, was responsible for final rod fracture (Yamanaka et al., 2015). According to Agarwal et al. studies (Agarwal et al., 2017, 2019), the stress distribution and stress amplitude depends on various factors including the scoliotic curvature and the loading conditions during the distraction events. According to their model, the stress in the rod reaches from 85 up to 810 MPa depending on the frequency and amplitude of the distractions and on the spine curvature. In a very recent study, Agarwal et al. discussed the link between high stress regions and fracture locations in dual-rod constructs (Agarwal et al., 2021). Based on finite element analysis (FEA), it was concluded that these regions coincide and are located on the posterior surface of the rods, close to the distal anchors and at mid construct level (Agarwal et al., 2021).

In the present study, we investigated broken growing rods removed after diagnosis of fracture. These rods are made of three different materials: Ti-6Al-4V alloy, pure Ti grade 2 (Ti Cp 2) and Co-Cr alloy. The specific construct used by our team is composed of a single-rod and is called the “3-hook & 2-screw” (H3S2) construct (Miladi and Mousny, 2014; Miladi et al., 2013). This construct is often selected for progressive scoliosis in skeletally immature patients. It involves no connector and a reserve located distally for future lengthening.

The first objective of the research is to unravel the mechanisms of fracture and to investigate the factors that control the failure process. The second objective is, based on the analysis of the failure mechanisms, to deduce strategies to guide towards novel practices that can reduce the risk of fracture. For this purpose, scanning electron microscopy is combined to X-ray analysis and to an analytical beam model to

determine the failure mechanisms as well as to estimate the magnitude of the forces at the origin of the fracture process. This analysis finally motivates the formulation of several failure mitigation strategies.

2. Materials and methods

2.1. Materials

Seven broken rods from three patients were analyzed. Patient “1” fractured one rod, patient “2” broke two rods and patient “3” broke four rods. The rods were rapidly removed after radiographic diagnosis. All patients were male treated for severe EOS, with mean age at first surgery of 8.1 years [6.2–10.9]. All three patients had a right thoracic primary structural curve according to Lenke classification (Lenke et al., 2001).

No patient had thoracic hyperkyphosis as the antero-posterior curvature of the thoracic spine was always in the range [10°–34°]. A H3S2 construct on a single sub-muscular growing rod was selected for each surgical procedure, as described by (Miladi and Mousny, 2014; Miladi et al., 2013). The CD Horizon® Legacy™ device (Medtronic, Memphis, TN) was used.

The Cobb angle is used to quantify the severity of the spine deformities. The patient is considered scoliotic when the Cobb angle exceeds 10°. The Cobb angle was corrected from 50° to 26° for patient “1”, from 48° to 43° for patient “2” and from 102° to 35° for patient “3”. The initial correction was maintained owing to rod lengthening (involving a surgical step) performed when a 10° increase of the Cobb angle was observed. The average number of instrumented vertebral segments was equal to 11 [10–13]. The mean duration between insertion and fracture was 13.9 months [4.8–29.6]. The mean body mass index (BMI) at surgery was 16.5 kg/m² [14.8–18]. Table 1 provides all relevant data about the H3S2 constructs and rod characteristics.

An additional rod made of the alloy Ti-6Al-4V with 5.5 mm

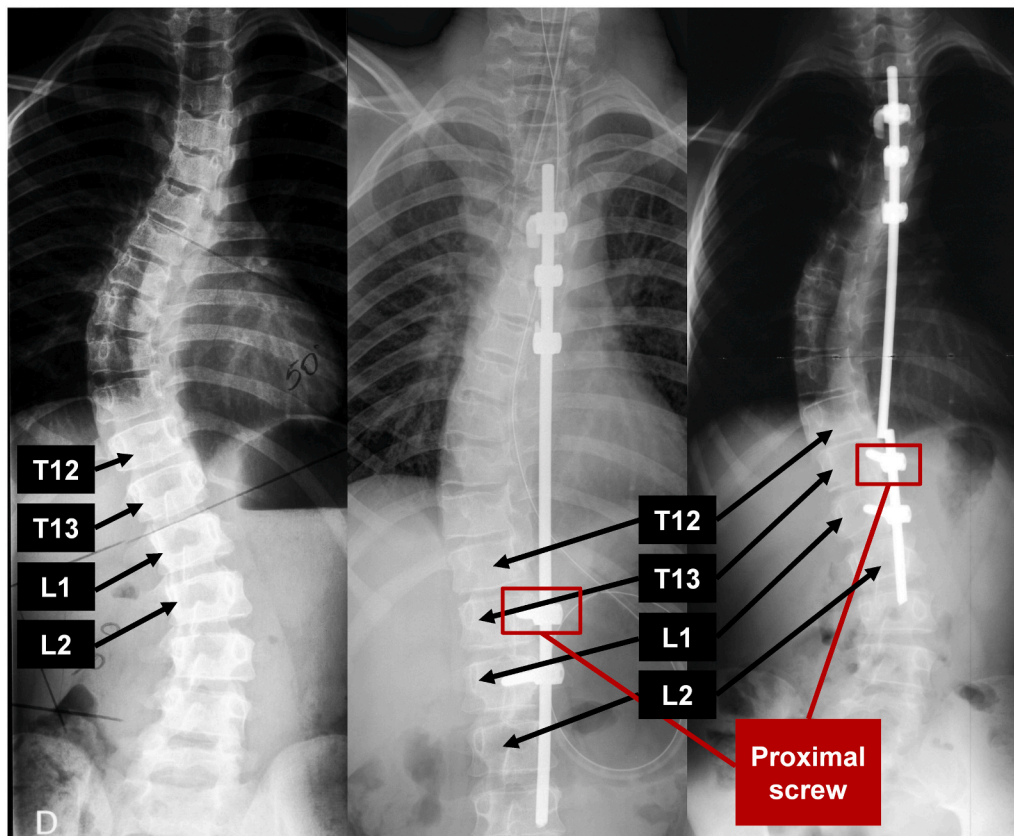


Fig. 1. X-ray of patient “1” with EOS before surgery (left), with H3S2 construct (middle) and rod failure (right).

Table 1

H3S2 constructs and rods characteristics. The rod materials are made of a titanium alloy Ti-6Al-4V, a pure titanium grade 2 (Ti Cp 2) and of a cobalt-chromium (Co-Cr) alloy. The H3S2 construct extends from thoracic (T) spine to lumbar (L) spine. The time elapsed between rod insertion and rod fracture (rod survival time) is given.

	Patient 1	Patient 2		Patient 3			Rod 4
		Rod 1	Rod 2	Rod 1	Rod 2	Rod 3	
Rod material	Ti Alloy	Ti Alloy	Ti Alloy	Ti Alloy	Ti Alloy	Ti Cp 2	Co-Cr
Rod diameter (mm)	5.5	5.5	5.5	5.5	5.5	6.35	5.5
Instrumented levels	from T5 to L2	from T4 to L1		from T3 to L3			
Rod survival time (months)	17.7	22.4	29.6	4.8	8.4	7.1	7.3

diameter, purchased from Medtronic Sofamor Danek under the trade name CD Horizon® Legacy™ System, was used to perform bending fatigue tests.

2.2. Methods

2.2.1. X-ray analysis

Posteroanterior (PA) and lateral X-rays, performed using a flat panel sensor (Konica) and a picture archiving and communication system for the archiving of the images (Carestream), were analyzed to identify the location of the crack initiation process. Five geometrical parameters, identified in Fig. 2, can be extracted from the post fracture X-ray radiography profile of the patients to be used in the beam model. The length of the spine (L_{spine}) is defined as the distance between the apexes of the lumbar lordosis and the cervical lordosis. The apexes of the spine are measured along a curved line passing through the center of each of the bodies of vertebrae (Fig. 2). The sagittal sinuosity of the spine (δ_{spine}) is defined as the distance between two parallel lines, one line being tangent to the two apexes of the lumbar and cervical lordoses and the other line being tangent to the apex of the dorsal kyphosis. X_1 is the distance between the apex of the lumbar lordosis and the proximal screw. X_{fract} is the distance between the proximal screw and the fracture location. L_{rod} is the distance between the proximal screw and the distal pedicular hook.

The post fracture X-ray radiography profiles of the patients were analyzed using *ImageJ* v1.48 software (ImageJ v1.48, 2014, NIH Image, USA) in order to determine the five parameters defined above. The scaling reference is the diameter of the rod given in Table 1. This

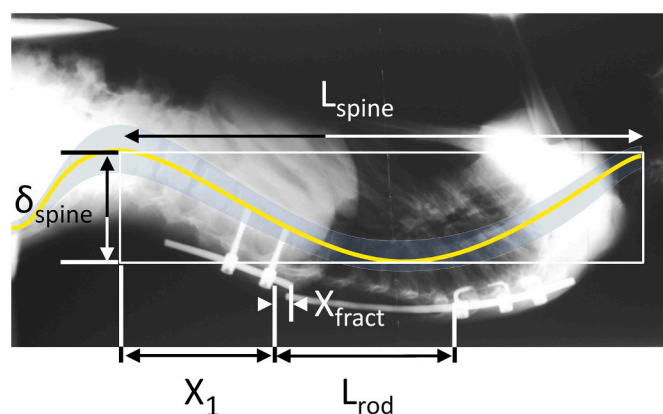


Fig. 2. Post fracture lateral X-ray radiography of patient 1 - 3th rod with the representation of the five characteristic lengths to be used in the beam model. The yellow line connects the center of vertebrae bodies.

reference is used to evaluate the conversion between the pixels and the real length.

2.2.2. Microstructure analysis

The microstructure of the three rod materials was characterized based on metallographic cross-sections taken parallel to the rod axis. The preparation involved the grinding and polishing with diamond suspensions followed by a 20-min silica suspension step for the Ti materials and by a 2-min alumina suspension step for the Co-Cr alloy. The titanium microstructures were revealed after etching, which consisted in 30-s immersion in a 3 mL HF, 6 mL HNO₃, and 91 mL water solution. The Co-Cr specimen was immersed 15 min in 40% HF, followed by a new 10-min alumina suspension polishing.

Micrographs were taken using scanning electron microscopy (SEM) (Ultra-55 FEG SEM, Carl Zeiss, Oberkochen, Germany). The three materials were characterized using backscattered electron detector (AsB) with an acceleration voltage of 20 kV.

2.2.3. Fracture surface analysis

Both pieces of in vivo fractured rod were compared to the corresponding PA and lateral X-rays in order to determine the orientation of the fracture surface with respect to the patient. All samples were cut 1 cm away from the fracture site using a water cooled saw (RGA commodore 300, Meylan, France). The fracture surfaces were analyzed by SEM. The SEM images were compared to PA and lateral X-rays to correlate with the direction of the forces acting on the rod.

2.2.4. Fatigue tests

Prior to the laboratory fatigue tests, a Ti-6Al-4V rod was cut into three specimens of 10 cm length and subsequently bent by a surgeon using a French rod bender following the surgical practice as closely as possible. Bending angles were measured with a profile projector (Mitutoyo PJ 300, Illinois, USA). The specimens were bent with different angles equal to 4°29', 10°32' and 13°02'.

The fatigue tests were performed on a hydraulic testing machine (Dartec, 15 kN) using the three-point bending setup shown in Fig. 3. The bending setup has three cylindrical supports with a diameter of 6.35 mm. The span between the two lower external supports was fixed at 4 cm.

Force-controlled experiments were carried out at a frequency of 10 Hz on all samples. The loading conditions were set to reach a maximum stress inside the rod varying from 10 to 90% of the yield stress of the material, i.e. 100–900 MPa, giving an *R* ratio equal to 1/9. The number

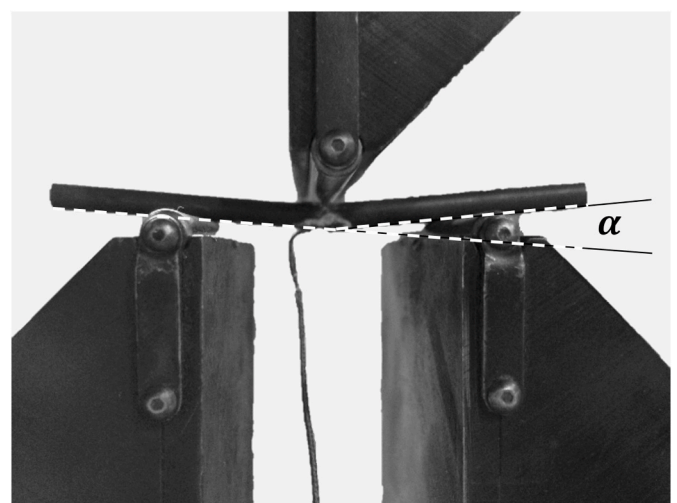


Fig. 3. Three-point fatigue bending setup with a sample bent at an angle α using a French bender prior to fatigue test. The span is equal to 40 mm. Self-heating was monitored to avoid variations of more than 5 °C in the central part.

of cycles to failure was determined when detecting a sudden variation in crosshead displacement at fracture event and was rounded to the nearest thousand.

3. Results

3.1. Microstructures of the three rod materials

The microstructures of the three materials presented in Fig. 4 correspond to cross-sections taken parallel to the rod axis (= horizontal direction in the micrographs).

Fig. 4a shows that the Ti-6Al-4V alloy is made of two phases: an α matrix composed of isotropic grains with a mean grain size of 3 μm together with smaller elongated β grains with a mean grain size of 0.5 μm . The volume fraction of the β phase is equal to $\sim 5\%$. In the case of the Ti Cp 2 (Fig. 4b), the microstructure is equiaxed with a mean grain size of about 10 μm . Most grains at the rod surface present twins, as shown in Fig. 5, which indicates a plastic accommodation associated to a shot peening process often used to increase fatigue resistance (Almen,

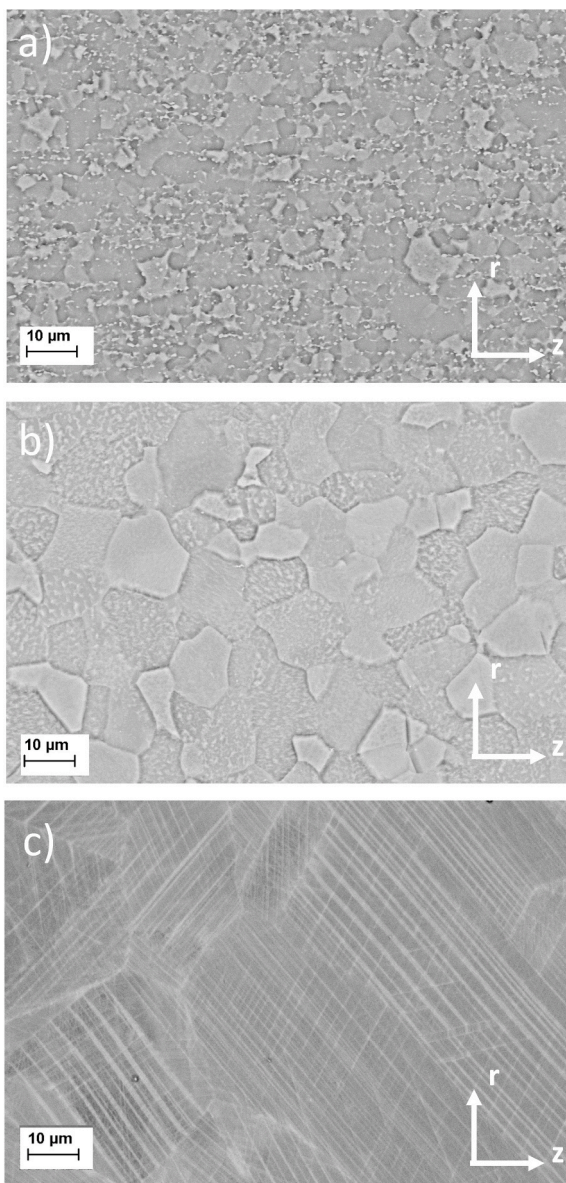


Fig. 4. SEM micrographs of axial microstructures from rods made of (a) Ti-6Al-4V alloy, (b) Ti Cp 2 and (c) Co-Cr alloy.

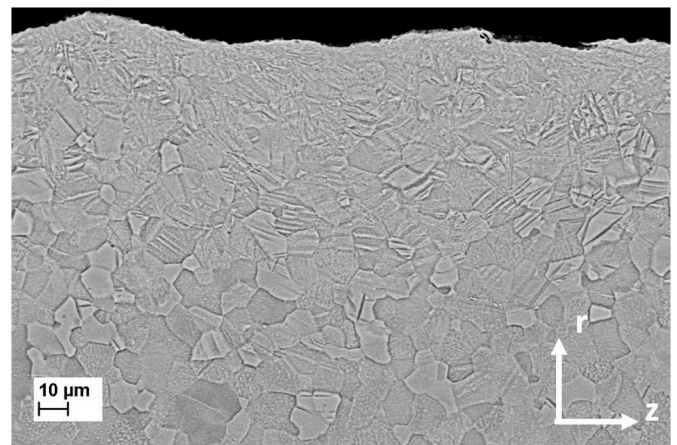


Fig. 5. SEM micrograph of twins at rod surface of Ti Cp 2.

1943). Finally, the Co-Cr alloy also presents equiaxed grains with an average size close to 40 μm with twins present over the entire diameter (see Fig. 4c). The equiaxed microstructure is obtained by thermal treatment after wire-drawing/extrusion process.

3.2. X-ray characterization

Table 2 reports the location of fracture initiation for each patient extracted from the X-ray images. Table 3 summarizes the values of the characteristics lengths measured as explained in the methods section and of the average for all seven patients. Individual patient's data are provided in Appendix.

3.3. SEM fractography of in vivo broken rods

3.3.1. Ti-6Al-4V

Fig. 6 shows typical fracture surfaces of Ti-6Al-4V rods. The five Ti-6Al-4V rods involve similar fracture patterns.

Fig. 7a shows that the surface is covered by curved and striated marks known as “clamshell marks”. These constitute the usual imprints of successive arrests of a propagating fatigue crack. Other lines, only found on the dorsal side, originate from the posterior surface and align perpendicular to the clamshell marks. These lines are called “ratchet marks” (see also Fig. 6), indicating the intersection locus of two cracks propagating in different planes (Otegui, 2014) and proving thus the existence of multiple crack initiation sites (Milella, P.P., 2012). Four out of the five rods exhibit a slant region, on both left and right sides. These so-called “shear lips”, observed in Fig. 6, develop when a crack approaches a surface due to plastic localization in 45° inclined bands (Milella, 2012) and lead to a shear-type ductile mechanism.

In the center, the clamshell profile evolves into a set of striations covered with small dimples as observed in Fig. 7b and known as “fatigue dimples”. This pattern indicates a transition of the fatigue propagation mechanism (Griebel, A., 2009), to a low-cycle fatigue mechanism caused by ductile void grow. This last mechanism involves relatively large crack advance at each cycle, quite similar to a static ductile failure

Table 2

Fracture location expressed as spine level, including thoracic (T), lumbar (L) and intervertebral disk (IV disk).

	Patient 1	Patient 2		Patient 3			
		Rod 1	Rod 2	Rod 1	Rod 2	Rod 3	Rod 4
Fracture location	T12-T13 IV disk	T12	T12	L2	L1	T11- T12 IV disk	T12-L1 IV disk

Table 3

Average values with standard deviations of the five characteristic lengths (see Fig. 3) extracted from X-ray for the 7 patients. All distances are given in centimeters.

δ_{spine} (cm)	L_{spine} (cm)	X_1 (cm)	L_{rod} (cm)	X_{fract} (cm)
5.5 ± 1.1	35.9 ± 2.1	9.0 ± 1.0	14.3 ± 1.7	1.9 ± 1.8

mechanism. On the ventral side, the curvature of the clamshell marks progressively changes, leading to the final fracture zone, see Fig. 7c.

3.3.2. Ti Cp 2

The fracture surface corresponding to a Ti Cp 2 rod shown in Fig. 8 exhibits ratchet marks on the dorsal side as well as clamshell marks. Lines perpendicular to clamshell marks were also observed, originating from the crack initiation site. These so-called “river marks”, similar to ratchet marks, indicate the confluence of different crack propagation planes (Otegui, 2014). The final fracture zone exhibits a small shear lip between the ventral side and the left side.

3.3.3. Co-Cr

A long ratchet mark can be observed on fracture surface of the Co-Cr

shown in Fig. 9, starting in the middle of the dorsal region and ending near the rod center.

As indicated in Fig. 10a, river marks can be found on both sides of the ratchet marks with small striations. The rest of the fracture surface exhibits a flat topography suggesting that the propagation direction was repeatedly deviated. The intermediate magnification of Fig. 10b reveals transverse cracks and higher magnification (Fig. 10c) shows striations parallel to each other, with direction varying from one grain to another. This indicates a relatively brittle transgranular fatigue mechanism.

The comparison between the SEM micrographs with the corresponding PA and lateral X-rays shows that, in all investigated rods, cracking initiates on the dorsal side and propagates towards the ventral side, with a tendency to deviate along the left side (bottom images in Figs. 6, 8 and 9).

3.4. Laboratory fatigue tests

The number of cycles to fracture was extracted from laboratory fatigue bending tests performed on Ti-6Al-4V rod specimens under a maximum stress equal to 90% of the yield stress. Fracture occurs after 369,000, 162,000, and 163,000 cycles for bending angles equal to 4°, 10° and 13°, respectively.

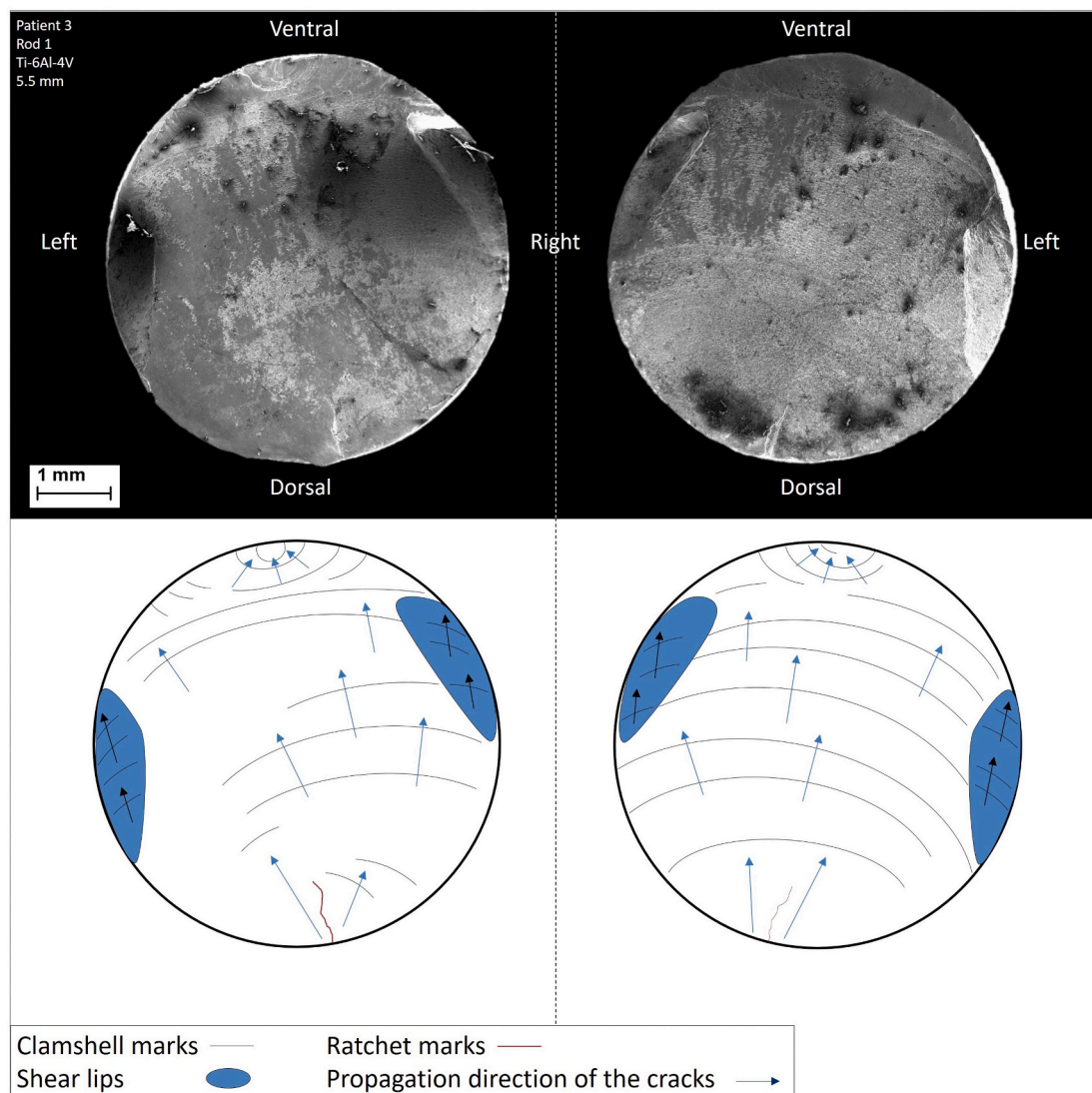


Fig. 6. Top image: SEM micrographs of the fracture surfaces of a broken Ti-6Al-4V rod. The lower part of the broken rods is on the left, the mating counterpart is on the right. Bottom image: schematic representation of the spreading of the fatigue cracks along the two corresponding fracture surfaces.

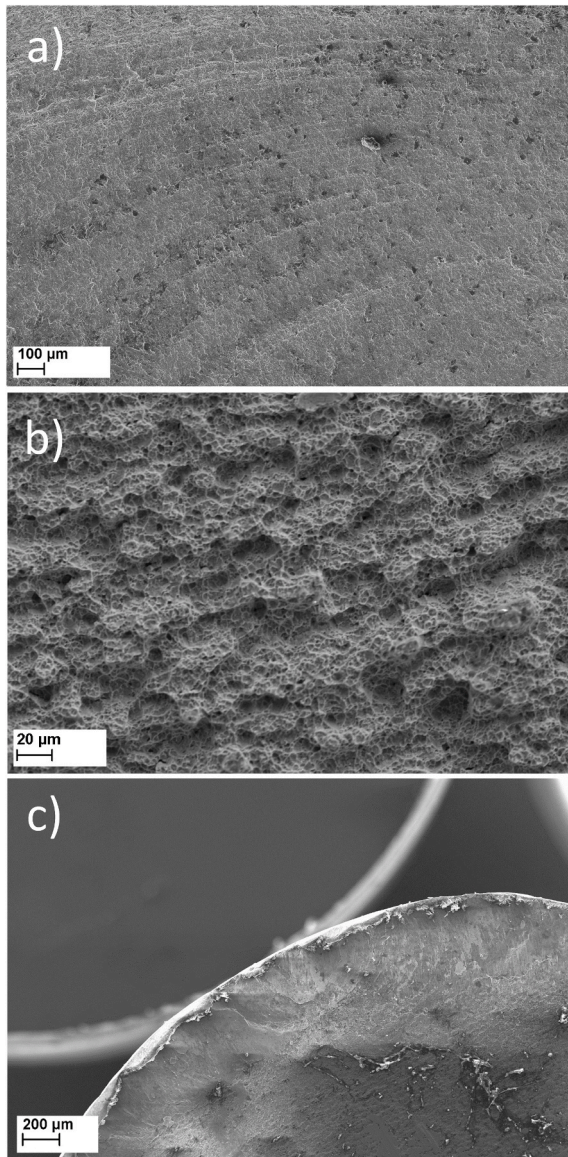


Fig. 7. SEM micrographs of the fracture surface of a broken Ti-6Al-4V alloy rod; (a) clamshell marks in the dorsal side of the surface of the rod; (b) fatigue ductile dimples between the two shear lips; (c) inversion of the clamshell marks curvature surrounding the final fractured zone in the ventral side of the rod.

Fractographies of the broken 10° bent rod are presented in Fig. 11. No ratchet marks are observed close to the initiation site. The fracture surface involves an area covered with beachmarks (Fig. 11c), expressing a relatively brittle mechanism of initiation during the first stage of the fatigue process, followed by larger striations covered with dimples (Fig. 11d), indicating a transition to a more ductile low-cycle fatigue failure mechanism. Finally, shear lips are present on both sides. The mechanisms are quite similar to the one observed in the in vivo rods, especially for the low-cycle fatigue part.

4. Analytical beam bending model of the spine

The model considers a healthy spine with no scoliosis. The shape of the spine between the apex of the lumbar lordosis and the cervical lordosis is approximated, as shown in Fig. 12, by a perfect sinusoidal function with a periodicity equal to L_{spine} and an amplitude equal to $\delta_{spine}/2$:

$$\delta(x) = \frac{\delta_{spine}}{2} \cos\left(\frac{2\pi}{L_{spine}}(x + X_1)\right). \quad (1)$$

The rod is approximated by a beam with a circular section of radius R_{rod} . The rod follows the sinusoidal shape of the spine between the upper proximal screw and the distal hook. The lower fixation of the rod in the lumbar vertebra is approximated by an embedment acting with a vertical force F_{v1} , a horizontal force F_{h1} and a bending moment M_1 . In the same way, the upper fixation imposes a vertical force F_{v2} , a horizontal force F_{h2} and a bending moment M_2 . Due to the mobility of the hooks in the upper fixation, M_2 is considered negligible and taken equal to zero. The rod is assumed defect free with no stress concentrator.

Using classical beam bending theory and applying the equilibrium conditions (the complete derivation is given in Supplementary material), the tensile stress on the dorsal side of the rod is equal to

$$\sigma_{surf}(x) = \frac{F_{v2}R_{rod}}{I_{rod}} \left[\frac{M_2}{F_{v2}} + \delta(L_{rod}) - \delta(x) + \frac{F_{h2}}{F_{v2}}(L_{rod} - x) \right] - \frac{F_{v2}}{A_{rod}}, \quad (2)$$

where I_{rod} is the second moment of inertia of the rod equal to $\pi R_{rod}^4 / 4$, and the cross-section area of the rod A_{rod} is given by $A_{rod} = \pi R_{rod}^2$. By differentiating Equation (2) with respect to x , the position of the maximum tensile stress ($x_{\sigma max}$), is found by solving

$$\frac{F_{h2}}{F_{v2}} = \frac{\delta_{spine}}{2} \frac{2\pi}{L_{spine}} \sin\left(\frac{2\pi}{L_{spine}}(x_{\sigma max} + X_1)\right). \quad (3)$$

As a first lower bound approximation, we assume that fracture occurs at the position corresponding to the maximum tensile stress ($x_{fract} = x_{\sigma max}$) when the tensile stress along the dorsal part of the rod reaches the fatigue endurance limit σ_{end} of the rod material (i.e. when $\sigma_{max} = \sigma_{end}$). Equation (3) gives the ratio of the two critical forces (F_{h2} and F_{v2}) that would potentially lead to fracture of the rod. From this ratio, one can estimate their intensities from (with $M_2 = 0$)

$$F_{v2} = \frac{\sigma_{end}}{\frac{R_{rod}}{I_{rod}} \left(\delta(L_{rod}) - \delta(x_{fract}) + \frac{F_{h2}}{F_{v2}}(L_{rod} - x_{fract}) \right) - \frac{1}{A_{rod}}}. \quad (4)$$

The endurance limit is a material property that depends on a large number of parameters related, among others, to the processing conditions and to the resulting microstructure, surface state, temperature, and/or presence of internal stresses. The endurance limit defined at 10^7 cycles is equal to 655 ± 136 MPa for Ti-6Al-4V (Akahori and Niinomi, 1998; CES Selector, 2016; Chao and López, 2007; Costa et al., 2006; Lin et al., 2005; Niinomi, 1998; Oguma and Nakamura, 2013; Okazaki, 2012; Rack and Oazi, 2006), to 286 ± 39 MPa for Ti Cp grade 2 (CES Selector, 2016; Donachie, 2000; Lin et al., 2005; Rack and Oazi, 2006), and to 462 ± 231 MPa for Co-Cr (Bayrak et al., 2010; CES Selector, 2016; Marrey et al., 2006; Niinomi, 1998; Okazaki, 2012; Rivard et al., 2013; Teoh, 2000). The uncertainty in the measurements and the dispersion on the values of σ_{end} have been taken into account through an error propagation analysis.

Knowing x_{fract} from post-fracture X-ray radiographies, F_{v2} and F_{h2} can be calculated for each patient by solving Eqns (3) and (4): F_{v2} varies from 171 to 424 N, and F_{h2} varies from 79 to 152 N. The mean value and the standard deviation of F_{v2} and F_{h2} are presented in Fig. 13.

An interesting outcome of the model is the possibility to predict the risk of failure of a construct and the position of the maximum stress in a rod directly from the geometrical data extracted on a X-ray radiography (δ_{spine} , L_{spine} , X_1 , L_{rod}) and on the forces acting on the rod (F_{v2} and F_{h2}). If F_{v2} and F_{h2} are known, the location of the point of maximum stress in the rod ($x_{\sigma max}$) can be calculated using Eqn (3). Due to the periodicity of the sinus function, solving Eqn (3) leads to a multiplicity of solutions for $x_{\sigma max}$ and one should carefully select the appropriate one.

This approach was used to predict the position of the maximum stress in a rod and the amplitude of the maximum stress for a hypothetical patient with geometrical dimensions taken as an average of the 3 pa-

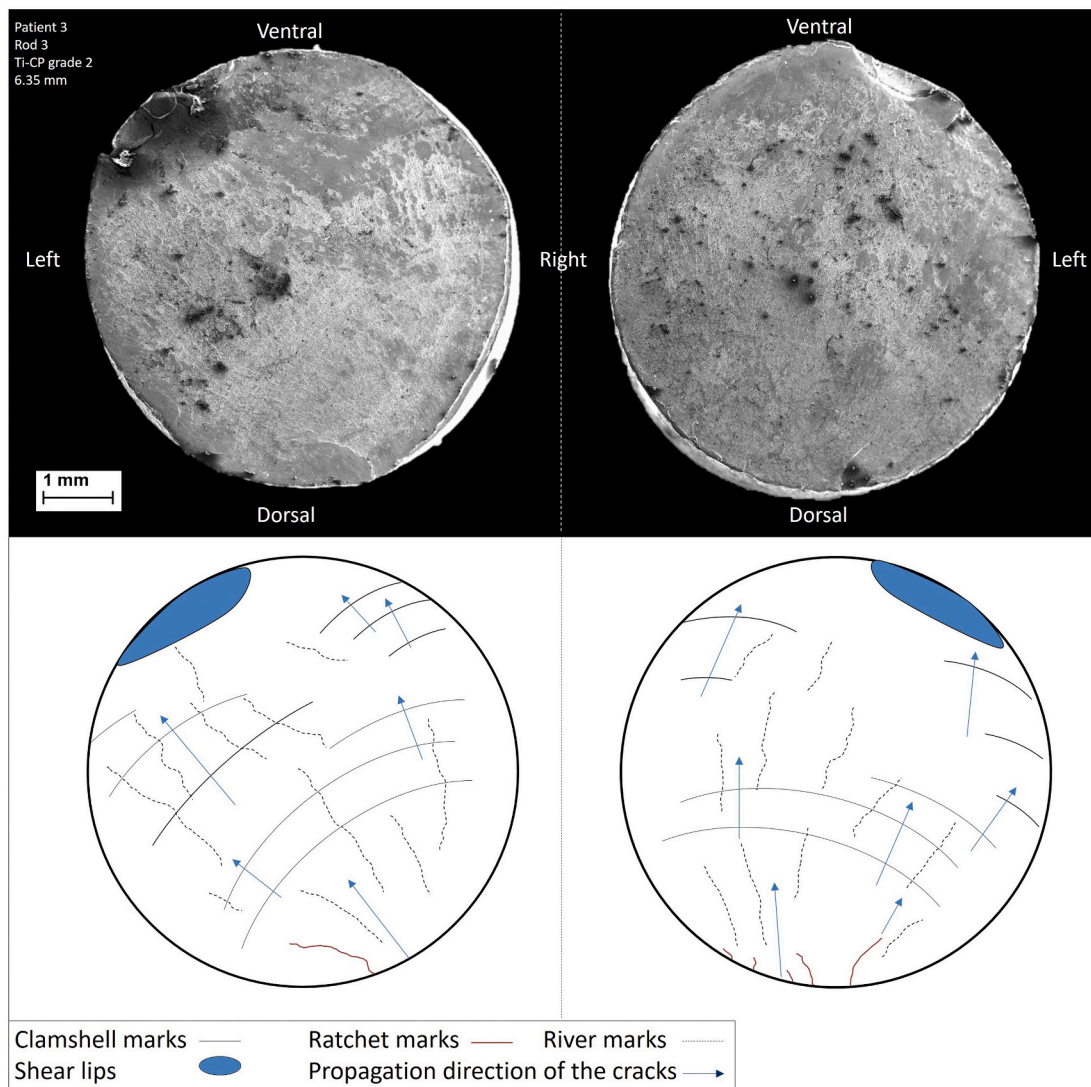


Fig. 8. Top image: SEM micrographs of the fracture surface of a broken pure titanium rod. The lower part of the broken rod is on the left, the mating counterpart is on the right. Bottom image: schematic representation of the spreading of the fatigue cracks along the two corresponding fracture surfaces.

tients of this study ($\delta_{spine} = 5.5$ cm, $L_{spine} = 36$ cm, $X_1 = 9$ cm and $L_{rod} = 14$ cm). The variation of the maximum stress on the dorsal side of the rod as a function of F_{v2} and F_{h2} is shown in Fig. 14 along with the endurance limit of the three materials investigated in this study.

The horizontal forces have a larger influence on the attainment of a critical stress state in the rod compared to the vertical force. This phenomenon is due to a lever effect and is proportional to the lever ratio L_{rod}/δ_{rod-0} , δ_{rod-0} being defined as $\delta(L_{rod}) - \delta(0)$, which is roughly equivalent to the ratio L_{spine}/δ_{spine} .

The model addressed above aimed at representing the mechanical response of a rod in a H3S2 construct in the sagittal plane. The estimates are based on X-ray measurements and fractography analysis. The model has several limitations such as: (i) the residual stress field and the indentation marks coming from the contouring process are not taken into account, neither stress concentrations close to anchorages; (ii) M_2 is neglected because hooks are used at the top fixation systems, while this hypothesis would become incorrect if only screws were used; (iii) torsion motions were not considered but fractographies indicate that failures were dominated by anteroposterior bending; (iv) the spine curve between the apex of the lumbar lordosis and the cervical lordosis in the sagittal plane is approximated by a perfect sinusoidal function; (v) the spine deformation in the frontal plane, i.e. Cobb angle, is not considered because the model only represents the rod geometry, and the rods are

mainly bent in the sagittal plane, being straight in the frontal plane; (vi) stresses resulting from spine growth are not taken into account. Considering these limitations, the predictions should only be taken as semi-quantitative. Nevertheless, even though the considered constructs were not identical, the predicted critical forces are in agreement with results from previous studies (Agarwal et al., 2019; Noorden et al., 2011; Serhan et al., 2013; Teli et al., 2012).

5. Discussion

5.1. Lifetime of the rods

The present investigation indicates that growth rods fail by fatigue as a result of everyday solicitation related to basic movements such as sitting, playing, or getting dressed. In order to evaluate the solicitation frequency, the number of cycles up to failure should be divided by the rod lifetime. In our study, the resistance of Ti-6Al-4V rods tested in kyphotic configuration was around 200,000 cycles. Piovesan et al. performed four-point bending fatigue tests on similar rods. In kyphotic configuration, rods run-out 10^6 cycles without failure for a maximum stress level of 577 MPa. In lordotic configuration, rods break after 2.4×10^4 cycles for a maximum stress level of 944 MPa (Piovesan et al., 2019). Stresses acting in vivo are not as regular as in laboratory fatigue tests.

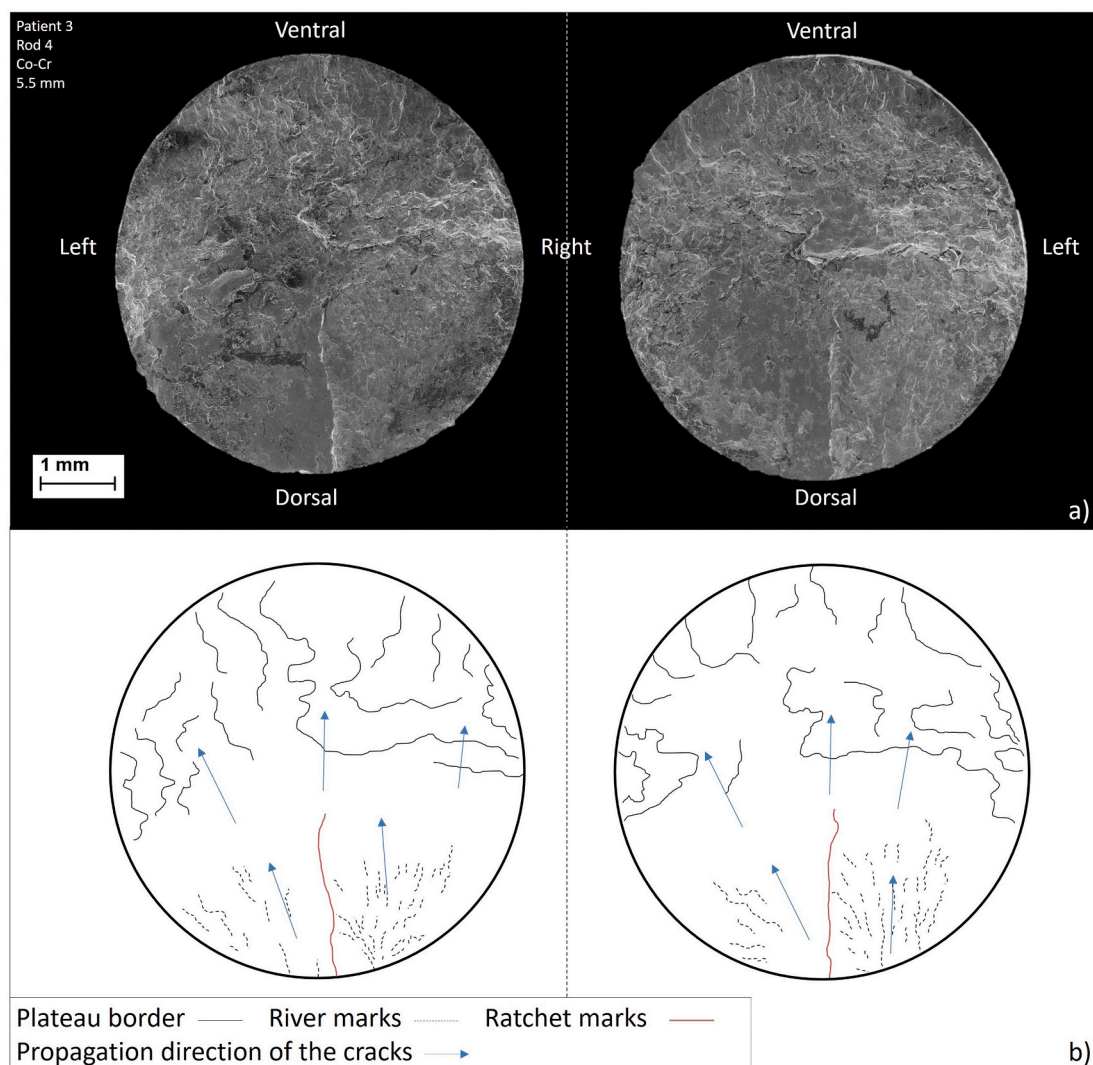


Fig. 9. Top image: SEM micrographs of the fracture surface of a broken Co-Cr alloy rod. The lower part of the broken rod is on the left, the mating counterpart is on the right. Bottom image: schematic representation of the spreading of the fatigue cracks along the two corresponding fracture surfaces.

We may consider that fatigue solicitation is a combination of low and high stresses. Our fatigue tests invariably induced 900 MPa in Ti-6Al-4V rods, which is a high-stress level not far from the yield stress. 2×10^5 cycles is thus probably a lower bound on the number of cycles. The average lifetime of the seven broken rods after implantation is 14 months. Only seven rods have been considered for estimation of the average lifetime. Yang et al. found a larger average time before fracture after initial insertion, of 25 ± 21 months, considering eighty-six broken rods (Yang et al., 2011). Assuming that the forces used during fatigue tests are of the same order of magnitude as the one in the back of the child, this is equivalent to a mechanical solicitation every 3 min associated to a bending moment of 14.7 Nm applied to the rod. On this basis, solicitations playing a role on setting the fatigue lifetime should occur over a time scale of the order of a few minutes. A smaller frequency would have been linked to occasional high intensity events, such as coughing or vomiting (Waugh, T.R., 1966), whereas a higher frequency would depict events occurring every second such as breathing. The obtained frequency fits classical movements such as walking, squatting, jumping, which are regular movements in a child's life.

The four broken rods in patient "3" exhibit a survival time shorter than for the two other patients. This cannot be explained by a higher BMI, nor by severe thoracic kyphosis (i.e. excessive outward curvature of the spine). The high percentage of scoliosis correction could be a

predisposing factor but this was not investigated in our study.

5.2. Failure location

Thoracolumbar junction is an at-risk location due to stress concentration. Smith et al. evaluated 30 patients with symptomatic rod fracture after posterior instrumented fusion for adult spine deformity, with most fractures occurring in the lumbar spine or thoracolumbar junction (Smith et al., 2012). 35 of the 86 rod fractures analyzed by Yang et al. occurred in that region as well (Yang et al., 2011). Agarwal et al. concluded, using FEA, that at-risk failure regions are close to distal anchors and at mid construct in dual-rod constructs. From X-ray radiography analyses, it was found that all rods but one (rod 1, patient "3") broke at the thoracolumbar junction. In patient "3", rod 1 failed at the level of L2, close to the thoracolumbar junction. Even if the type of growing rod construct can influence the location of the fracture initiation site, thoracolumbar is certainly an at-risk location.

The fatigue cracks always initiate from the dorsal side of the rod and propagate towards the ventral side, with a tendency to slightly deviate towards the left side. This suggests that the rods break mainly because of repeated action of a bending moment in the anteroposterior direction. Piovesan et al., compared residual stresses in kyphotic and lordotic conditions. At thoracolumbar junction, rods are usually bent in lordotic

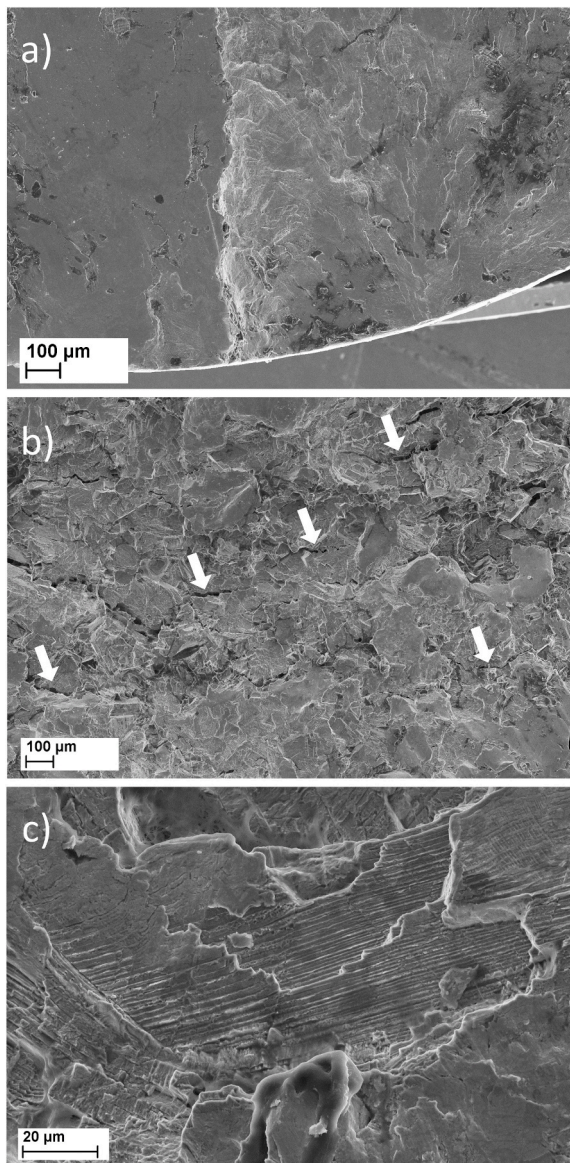


Fig. 10. SEM micrographs of the fracture surface of a broken Co-Cr alloy rod; (a) river marks on the dorsal side of the surface of the rod; (b) transverse cracks from the center of the surface to the ventral side of the rod; (c) fatigue striation at the scale of a single grain exhibiting a stair-step morphology.

configuration. In this configuration, the stress state along the dorsal side results from two tensile contributions: residual stresses induced by the contouring process and extra stress induced by anterior flexion loading (Piovesan et al., 2019). Tensile residual stresses favor crack initiation, reducing rod lifetime. The bending process induces residual stresses leading to an effective decrease of the fatigue resistance in the thoracolumbar region. Residual stress after rod bending affects rod fatigue performance (Slivka et al., 2013). As the spine experiences higher and more frequent loads in flexion (White and Panjabi, 1990), rods contoured in lordosis and inserted at thoracolumbar junction or in lumbar spine would thus be more susceptible to fatigue cracking due to residual stresses contribution (Piovesan et al., 2019).

5.3. Fatigue mechanisms

Multiple initiation sites are activated due to imperfections at the rod surfaces. Fatigue cracks usually initiate in areas subjected to the largest cyclic tensile stress. In addition, defects such as surface roughness,

indentation, pre-cracks, inclusions, or porosity favor crack initiation by acting as stress concentrators (Suresh, 1998). These defects mostly originate from the manufacturing process (Yamanaka et al., 2015; Yoshihara, 2013). Additional defects can be subsequently introduced during rod contouring and manipulation by the surgeon (Demura et al., 2015; Yoshihara, 2013). Bending instruments such as the French rod bender and the in situ bender are known to introduce shallow notches, affecting the fatigue resistance (Dick and Bourgeault, 2001; Lindsey et al., 2006; Yoshihara, 2013). The connection between the rod and the screws or hooks also creates permanent marks (Yoshihara, 2013). The ratchet marks on the dorsal side of each rod denote the presence of multiple initiation sites. No ratchet mark was found on laboratory fatigue rod fractography. In the studied laboratory configuration, crack initiates along the convex side of the rod. The surface on that side of the laboratory fatigue specimens can be assumed defect-free as no indentation marks were induced in this area during the bending process.

The Ti-6Al-4V rods all show evidences after initiation of striations, typical of a crack tip plasticity induced fatigue mechanism, followed by a low-cycle fatigue ductile stage and a final tearing step, independent of composition and diameter. In all materials, the final ductile tearing process occurs when the crack is sufficiently long for the stress intensity factor to reach the fracture toughness under a particularly severe load excursion. This is consistent with previous studies on different spinal constructs, e.g. Harrington rods (Stürz et al., 1979), Harrington rod cervical stent (Reitz, 2013), and posterior rods (Yamanaka et al., 2015). Only the Co-Cr rod does not show the same plastic void growth dominated failure stage.

Leaving aside the detrimental effect of the marks and surface defects (that can potentially be mitigated), our calculations show that the observed failures cannot be attributed to particular internal materials defects or to non-expected microstructure problems, but are the consequences of the cyclic stresses generated in daily life which reach, at reasonable force levels, the expected endurance limit.

5.4. Loading

The anteroposterior forces have different origins. Distraction is used to maintain the correction of scoliosis, independent of the construct (Thompson et al., 2007; Yazici and Olgun, 2013). The force required to straighten the spine is transferred to the rod as a compressive and bending stress. The spine “pushes” on the rod with a force that depends on the correction amplitude. Teli et al. showed a linear relationship between this vertical force and the distraction needed for scoliosis correction (Teli et al., 2012). Waugh added the effect of vertical forces during day-to-day movements (20% increase while sitting and standing up), with peaks during involuntary movements like coughing (206% increase) and vomiting (490% increase) (Waugh, 1966). Day-to-day physical activities of a child (walking, running, jumping ...) are expected to increase in a cyclic way these vertical forces. These forces, acting in a direction parallel to the rod axis, are due to the constraint necessary to hold the correction of the scoliotic curve and to resist gravity. Associated, bending moment in the anteroposterior direction may also occur because of anterior flexion movement of the spine. In our research, all three patients had a right thoracic primary structural curvature without any thoracic hyperkyphosis. The vertical and horizontal forces, responsible for each rod failure, have the same general trend: vertical forces are two to three times larger than horizontal forces. However, the horizontal forces play a dominant role on maximum stress level due to a greater lever effect in the structure.

5.5. Rod diameter

The effect of rod diameter on their lifetime is uncertain. During the contouring phase, Slivka et al. explained in their study that a larger diameter leads to larger strains at the rod periphery for the same bending curvature, which negatively affects fatigue resistance as larger

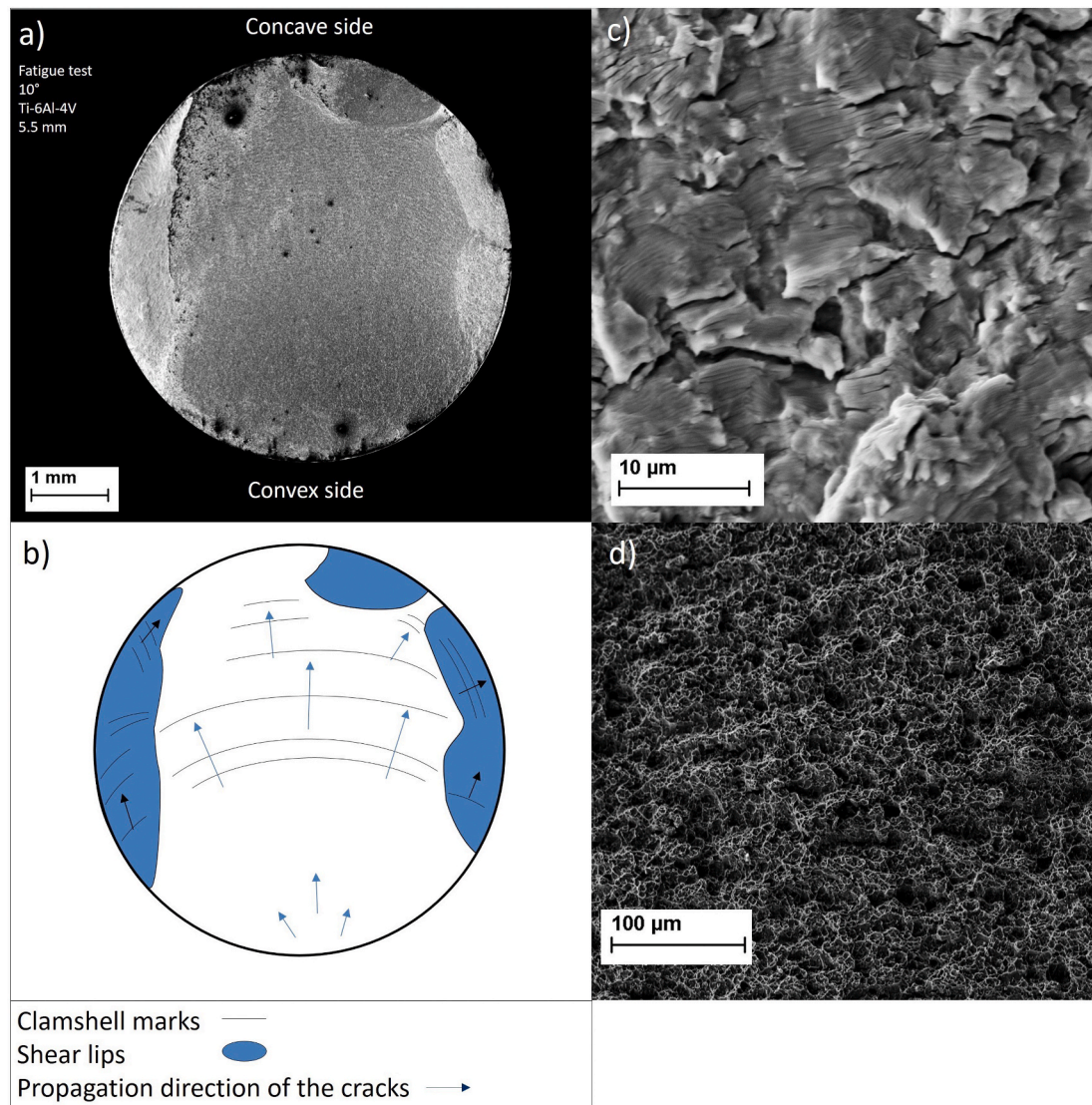


Fig. 11. (a) SEM micrographs of the fracture surface of a 10° bent rod after laboratory fatigue testing (Ti-6Al-4V alloy); (b) schematic representation of the spreading of the fatigue cracks; (c) fatigue striations close to initiation site; (d) fatigue ductile dimples between the two shear lips.

diameter rods are then more prone to fatigue crack initiation (Slivka et al., 2013). However, the same authors (Slivka et al., 2013) also pointed out that higher rates of fracture were associated to smaller diameters. As a matter of fact, the key question is whether daily activities are force/moment controlled or deflection/bending angle controlled. Force controlled activity is typical of carrying dead loads, but a flexure to reach an object is closer to deflection control. In our study, the effect of the radius of the rods was not investigated experimentally as only one radius was used for each rod material.

5.6. Materials choice

The clinical objective when using a non-fusion growth-rod technique is to minimize the risks of failure, as already identified in earlier studies (Yang et al., 2011; Smith et al., 2012). Fracture initiation is influenced by the defects and residual stresses induced by the manufacturing process and preoperative handling. Before being inserted in a patient, a rod is exposed to a succession of contouring combined, in some case, with indentation marking. After insertion in the patient, the rod is subjected to fatigue loading. As the bending moment in anteroposterior direction was identified as the main component responsible for fracture, wearing an anti-kyphosis brace could be seen as an alternative. But, a brace will

only decrease the bending forces due to anterior flexion movement of the spine. Therefore, it will, at best, delay fracture, but not prevent it.

Selecting materials with a higher fatigue endurance limit only is not sufficient to prevent rod failure nor does it guarantee a longer lifetime of the rod. Indeed, regarding patient “3”, while Ti-6Al-4V exhibits a larger endurance limit compared to Co-Cr rods, both were used and showed a similar lifetime. Some studies specifically investigated the fatigue life of contoured rods (Nguyen et al., 2011; Shinohara et al., 2016; Slivka et al., 2013; Smith et al., 2012; Yoshihara, 2013). Co-Cr rods showed superior fatigue performance compared to Ti alloys, but both lead to failure issues. The optimal material should thus have a high fatigue endurance limit and keep it after the contouring process.

The stiffness of the construct is also important to consider. As already touched upon above, there is still an uncertainty regarding the dominant (cyclic) loading mode of the rod by the patient. Whether it is mainly load-controlled (i.e. the patient applies a given force on the rod) or displacement controlled (i.e. the patient applies a given deflection on the rod) is not precisely known. If we assume that growth rods are being loaded in a displacement-controlled mode, the stiffness of the Co-Cr alloy (210–220 GPa) being larger than for the alloys Ti-6Al-4V (110–119 GPa) and Ti Cp 2 (100–105 GPa) (CES EduPack, 2019), the Co-Cr rod will undergo proportionally larger stresses (for similar

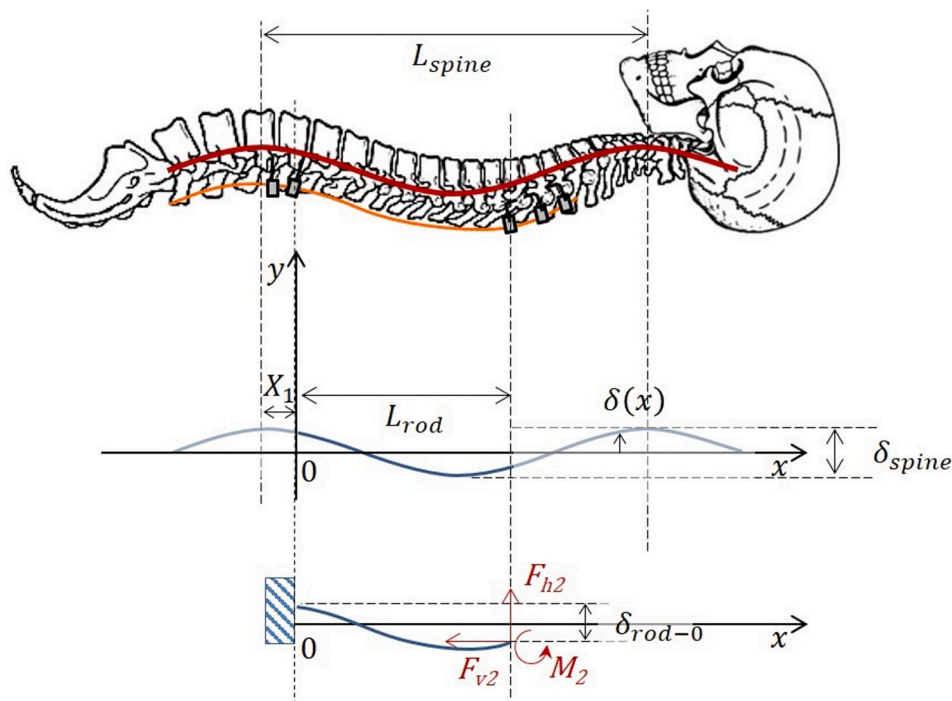


Fig. 12. Schematic representation of the spinal column model.

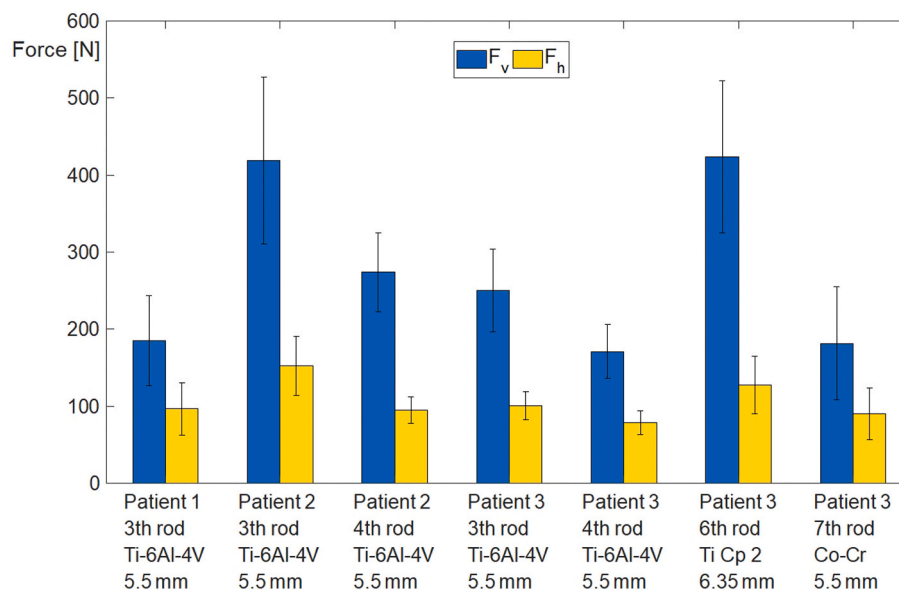


Fig. 13. Vertical and horizontal force responsible for the fatigue fracture of the rods calculated from the model at the x_{frac} position. The error bars represent the standard deviations.

diameter).

This illustrates the complexity of material selection for a growth rod application. A fail-safe material should have a high fatigue endurance limit, which is related to a high yield stress (the endurance limit is typically equal to 1/3 of the yield stress). A high yield stress makes the contouring process more difficult as the surgeons will need more force for bending and may worsen the indents and thus the defects favoring fracture initiation. Vice versa, a high yield stress guarantees the absence of plastic bending induced by the movements of the patient. A moderately low elastic modulus is preferable to favor an elastic behavior, but it should not be too low, otherwise the correction cannot be maintained (or at the expense of a very thick rod). Future developments should thus

focus on selecting new materials with higher strength, strong enough to hold the scoliosis correction, and compliant enough to allow enough spine mobility. This ideal material should resist marking, which means that no or minimum surface defect is induced by the rod contouring or by the connection to the screws and hooks. An option could be offered by new generations of metallic glasses with very high strength and large elastic deformation potential, but only if they can be made less brittle through different types of ductilization mechanisms (e.g. Pan et al., 2018).

In the meantime, alternative solutions exist to improve lifetime based on predictive patient specific models. One could adapt the rod geometry at the critical sites. Cui et al. (2010) indeed demonstrated

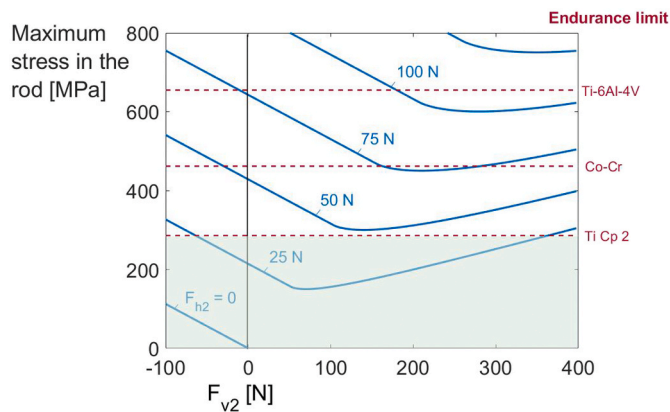


Fig. 14. Variation of the maximum stress in the dorsal side of the rod as a function of the imposed forces F_{h2} and F_{v2} at the upper hook for $R_{rod} = 5.5$ mm, $\delta_{spine} = 5.5$ cm, $L_{spine} = 36$ cm, $X_1 = 9$ cm and $L_{rod} = 14$ cm. The endurance limit of Ti-6Al-4V alloy, Ti Cp 2 and Co-Cr alloy is indicated in red. A positive value of the stress corresponds to a tensile stress. The green surface represents a safe zone for a rod made of pure Ti.

better biomechanical performance for square cross-section rods compared to circular cross-section rods. A second solution would be to use pre-contoured rods with internal stress relaxed by adequate thermal treatment or, alternatively, by compressive internal stress pre-induced at the predicted location. Development of advanced predictive models to guide practice optimization is currently under study based on both finite element methods and fatigue tests.

6. Conclusions

Growing rod fracture is a major complication of fusionless surgeries used to treat early onset scoliosis. The fracture mechanism in seven growing rods from patients with early onset scoliosis and treated by H3S2 construct was analyzed relying on fractography, fatigue testing and beam theory. The main conclusions of the analysis are the following:

- Fracture occurs through classical fatigue mechanisms caused by a repeated bending in the anteroposterior direction, for all diameters and material types.
- Fracture generally initiates at the thoracolumbar, but various fatigue crack initiation sites were found on every rod, stemming from imperfections presumably induced by the manufacturing process and from rod contouring.

Appendix A. Patients' X-ray imaging characterization

- The vertical and horizontal forces predicted based on the beam model combined to the number of cycles to failure determined from the laboratory fatigue tests on pre-bent specimens indicate that the fatigue process is controlled by daily life activities taking place at frequency in the minutes to a few tens of minutes range.
- The failure risks can be decreased by wearing an anti-kyphosis brace, changing the intrinsic rod characteristics/materials (strength, compliance, resistance to marking), adapting rod geometry and/or inducing compressive stress at critical sites or using pre-contoured rods with internal stress relaxed.

Contribution of the authors

Conceptualization: Maryline Mousny, Pascal J. Jacques, Thomas Pardoen, Data curation: Maryline Mousny, Nadia Irda, Lotfi Miladi, Formal analysis: Arnaud Ribesse, Maryline Mousny, Funding acquisition: Thomas Pardoen, Maryline Mousny, Investigation: Arnaud Ribesse, Karim Ismail, Nadia Irda, Lotfi Miladi, Methodology: Arnaud Ribesse, Thomas Pardoen, Maryline Mousny, Project administration: Pascal J. Jacques, Thomas Pardoen, Maryline Mousny, Resources: Pascal J. Jacques, Thomas Pardoen, Maryline Mousny, Software: Supervision: Thomas Pardoen, Pascal J. Jacques, Maryline Mousny, Validation: Karim Ismail, Visualization: Nadia Irda, Lotfi Miladi, Roles/Writing - original draft: Arnaud Ribesse, Karim Ismail, Thomas Pardoen, Maryline Mousny, Writing - review & editing: Karim Ismail, Arnaud Ribesse, Maité Croonenborghs, Pascal J. Jacques, Thomas Pardoen, Maryline Mousny.

Funding

This work was supported by the FRIA grant of A.R. from the National Funds for Scientific Research (FRS-FNRS), and by UCLouvain through the assistant mandate of M.C.

Declaration of competing interest

The authors declare that they have no known competing financial interests or personal relationships that could have appeared to influence the work reported in this paper.

Acknowledgements

The authors would like to thank Dr. Pierre Bollen for his technical assistance for fracture surface analysis and Dr. Olivier Cartiaux for his involvement in the project and the supply of medical material.

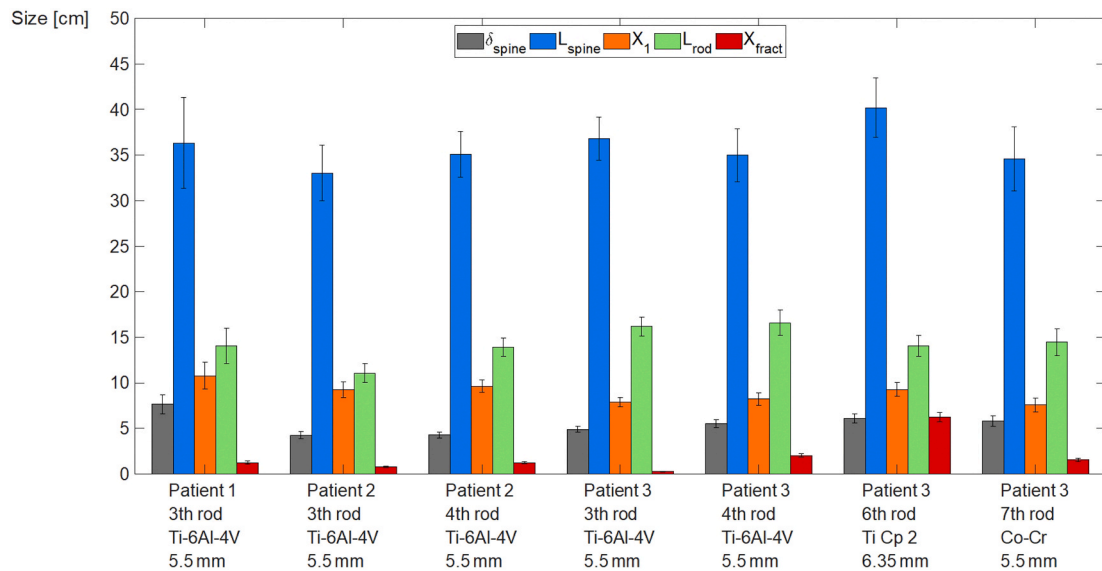


Figure A1. Geometrical characteristics of each patient.

Appendix B Supplementary data

Supplementary data to this article can be found online at <https://doi.org/10.1016/j.jmbbm.2021.104620>.

References

- Agarwal, A., Agarwal, A.K., Jayaswal, A., Goel, V.K., 2017. Outcomes of optimal distraction forces and frequencies in growth rod surgery for different types of scoliotic curves: an in silico and in vitro study. *Spine deformity* 5, 18–26. <https://doi.org/10.1016/j.jspd.2016.09.047>.
- Agarwal, A., Goswami, A., Vijayaraghavan, G.P., Srivastava, A., Kandwal, P., Nagaraja, U.B., et al., 2019. Quantitative characteristics of consecutive lengthening episodes in early-onset scoliosis (EOS) patients with dual growth rods. *Spine* 44, 397–403. <https://doi.org/10.1097/BRS.0000000000002835>.
- Agarwal, A., Kodigudla, M., Kelkar, A., Jayaswal, D., Goel, V., Palepu, V., 2021. Towards a validated patient-specific computational modeling framework to identify failure regions in traditional growing rods in patients with early onset scoliosis. *North American Spine Society Journal (NASSJ)* 5, 100043. <https://doi.org/10.1016/j.xnsj.2020.100043>.
- Akahori, T., Niinomi, M., 1998. Fracture characteristics of fatigued Ti-6Al-4V ELI as an implant material. *Mater. Sci. Eng., A* 243, 237–243. [https://doi.org/10.1016/S0921-5093\(97\)00807-1](https://doi.org/10.1016/S0921-5093(97)00807-1).
- Akbarnia, B.A., Emans, J.B., 2010. Complications of growth-sparing surgery in early onset scoliosis. *Spine* 35, 2193–2204. <https://doi.org/10.1097/BRS.0b013e3181f070b5>.
- Akbarnia, B.A., Marks, D.S., Boachie-Adjei, O., Thompson, A.G., Asher, M.A., 2005. Dual growing rod technique for the treatment of progressive early-onset scoliosis: a multicenter study. *Spine* 30, S46–S57. <https://doi.org/10.1097/01.brs.0000175190.08134.73>.
- Akgül, T., Dikici, F., Şar, C., Talu, U., Domaniç, Ü., 2014. Growing rod instrumentation in the treatment of early onset scoliosis. *Acta Orthop. Belg.* 80, 457–463.
- Almen, J.O., 1943. Shot blasting to increase fatigue resistance. *SAE Trans.* 248–268.
- Bayrak, Ö., Yetim, A.F., Alsarar, A., Çelik, A., 2010. Fatigue life determination of plasma nitrided medical grade CoCrMo alloy. *Fatig. Fract. Eng. Mater. Struct.* 33, 303–309. <https://doi.org/10.1111/j.1460-2695.2010.01442.x>.
- Bess, S., Akbarnia, B.A., Thompson, G.H., Sponseller, P.D., Shah, S.A., El Sebaie, H., Boachie-Adjei, O., Karlin, L.L., Canale, S., Poe-Kochert, C.R.N., Skaggs, D.L., 2010. Complications of growing-rod treatment for early-onset scoliosis: analysis of one hundred and forty patients. *J. Bone Joint Surg.* 92, 2533–2543. <https://doi.org/10.2106/JBJS.I.01471>.
- CES EduPack 2019, 2019. V 19.2.0. Granta Design Limited.
- CES Selector 2016, 2015. V 15.10.8. Granta Design Limited.
- Chao, J., López, V., 2007. Failure analysis of a Ti6Al4V cementless HIP prosthesis. *Eng. Fail. Anal.* 14, 822–830. <https://doi.org/10.1016/j.engfailanal.2006.11.003>.
- Costa, M.Y.P., Voorwald, H.J.C., Pigatin, W.L., Guimarães, V.A., Cioffi, M.O.H., 2006. Evaluation of shot peening on the fatigue strength of anodized Ti-6Al-4V alloy. *Mater. Res.* 9, 107–109. <https://doi.org/10.1590/S1516-14392006000100020>.
- Cui, Y., Lewis, G., Qi, G., 2010. Numerical analysis of models of the standard TSRH spinal instrumentation: effect of rod cross-sectional shape. *Comput. Methods Biomech. Biomed. Eng.* 5, 75–80. <https://doi.org/10.1080/10255840290008097>.
- Demura, S., Murakami, H., Hayashi, H., Kato, S., Yoshioka, K., Yokogawa, N., Ishii, T., Igarashi, T., Fang, X., Tsuchiya, H., 2015. Influence of rod contouring on rod strength and stiffness in spine surgery. *Orthopedics* 38, e520–e523. <https://doi.org/10.3928/01477447-20150603-61>.
- Dick, J.C., Bourgeault, C.A., 2001. Notch sensitivity of titanium alloy, commercially pure titanium, and stainless steel spinal implants. *Spine* 26, 1668–1672.
- Donachie, M.J., 2000. Titanium. A Technical Guide. Second Edition, vol. 105. ASM International.
- Griebel, A., 2009. Technical brief: fatigue dimples. *J. Fail. Anal. Prev.* 9, 193–196. <https://doi.org/10.1007/s11668-009-9228-z>.
- Hickey, B.A., Towriss, C., Baxter, G., Yasso, S., James, S., Jones, A., Howes, J., Davies, P., Ahuja, S., 2014. Early experience of MAGEC magnetic growing rods in the treatment of early onset scoliosis. *Eur. Spine J.* 23, S61–S65. <https://doi.org/10.1007/s00586-013-3163-0>.
- Lenke, L.G., Betz, R.R., Harms, J., Bridwell, K.H., Clements, D.H., Lowe, T.G., Blanke, K., 2001. Adolescent idiopathic scoliosis: a new classification to determine extent of spinal arthrodesis. *J. Bone Joint Surg.* 83, 1169–1181.
- Lin, C.W., Ju, C.P., Lin, J.H.C., 2005. A comparison of the fatigue behavior of cast Ti-7.5 Mo with cp titanium, Ti-6Al-4V and Ti-13Nb-13Zr alloys. *Biomaterials* 26, 2899–2907. <https://doi.org/10.1016/j.biomaterials.2004.09.007>.
- Lindsey, C., Deviren, V., Xu, Z., Yeh, R.-F., Puttlitz, C., 2006. The effects of rod contouring on spinal construct fatigue strength. *Spine* 31, 1680–1687. <https://doi.org/10.1097/01.brs.0000224177.97846.00>.
- Marrey, R.V., Burgermeister, R., Grishaber, R.B., Ritchie, R.O., 2006. Fatigue and life prediction for cobalt-chromium stents: a fracture mechanics analysis. *Biomaterials* 27, 1988–2000. <https://doi.org/10.1016/j.biomaterials.2005.10.012>.
- Miladi, L., Mousny, M., 2014. A novel technique for treatment of progressive scoliosis in young children using a 3-hook and 2-screw construct (H3S2) on a single sub-muscular growing rod: surgical technique. *Eur. Spine J.* 23, 432–437. <https://doi.org/10.1007/s00586-014-3339-2>.
- Miladi, L., Journe, A., Mousny, M., 2013. H3S2 (3 hooks, 2 screws) construct: a simple growing rod technique for early onset scoliosis. *Eur. Spine J.* 22, 96–105. <https://doi.org/10.1007/s00586-012-2379-8>.
- Milella, P.P., 2012. In: *Fatigue and Corrosion in Metals*. Springer Milan.
- Nguyen, T.Q., Buckley, J.M., Ames, C., Deviren, V., 2011. The fatigue life of contoured cobalt chrome posterior spinal fusion rods. *Proc. IME H J. Eng. Med.* 225, 194–198. <https://doi.org/10.1243/09544119JEM763>.
- Niinomi, M., 1998. Mechanical properties of biomedical titanium alloys. *Mater. Sci. Eng., A* 243, 231–236. [https://doi.org/10.1016/S0921-5093\(97\)00806-X](https://doi.org/10.1016/S0921-5093(97)00806-X).
- Noordeen, H.M., Shah, S.A., Elsebaie, H.B., Garrido, E., Farooq, N., Al Mukhtar, M., 2011. In vivo distraction force and length measurements of growing rods: which factors influence the ability to lengthen? *Spine* 36, 2299–2303. <https://doi.org/10.1097/BRS.0b013e31821b8e16>.
- Oguma, H., Nakamura, T., 2013. Fatigue crack propagation properties of Ti-6Al-4V in vacuum environments. *Int. J. Fatig.* 50, 89–93. <https://doi.org/10.1016/j.ijfatigue.2012.02.012>.

- Okazaki, Y., 2012. Comparison of fatigue properties and fatigue crack growth rates of various implantable metals. *Materials* 5, 2981–3005. <https://doi.org/10.3390/ma5122981>.
- Otegui, J.L., 2014. In: *Failure Analysis: Fundamentals and Applications in Mechanical Components*. Springer Cham International Publishing.
- Pan, J., Wang, Y.X., Guo, Q., Zhang, D., Greer, A.L., Li, Y., 2018. Extreme rejuvenation and softening in a bulk metallic glass. *Nat. Commun.* 9, 560. <https://doi.org/10.1038/s41467-018-02943-4>.
- Patterson, J.F., Webb, J.K., Burwell, R.G., 1990. The operative treatment of progressive early onset scoliosis. A preliminary report. *Spine* 15, 809–815.
- Piovesan, A., Berti, F., Villa, T., Pennati, G., La Barbera, L., 2019. Computational and experimental fatigue analysis of contoured spinal rods. *J. Biomech. Eng.* 141 <https://doi.org/10.1115/1.4042767>.
- Rack, H.J., Qazi, J.I., 2006. Titanium alloys for biomedical applications. *Mater. Sci. Eng. C* 26, 1269–1277. <https://doi.org/10.1016/j.msec.2005.08.032>.
- Reitz, W., 2013. Cervical stent failure analysis. *J. Fail. Anal. Prev.* 13, 678–683. <https://doi.org/10.1007/s11668-013-9749-3>.
- Rivard, K., Craft, A., Smith, T., Aboud, B., 2013. Qualification of hot isostatic pressing processes. In: *Medical Device Materials VI: Proceedings from the Materials and Processes for Medical Devices Conference (MPMD 2011)*. ASM International, p. 69.
- Sankar, W.N., Acevedo, D.C., Skaggs, D.L., 2010. Comparison of complications among growing spinal implants. *Spine* 35, 2091–2096. <https://doi.org/10.1097/BRS.0b013e3181c6edd7>.
- Serhan, H., Mhatre, D., Newton, P., Giorgio, P., Sturm, P., 2013. Would CoCr rods provide better correctional forces than stainless steel or titanium for rigid scoliosis curves? *Clinical Spine Surgery* 26, E70–E74. <https://doi.org/10.1097/BSD.0b013e31826a0f19>.
- Shinohara, K., Takigawa, T., Tanaka, M., Sugimoto, Y., Arataki, S., Yamane, K., Watanabe, N., Ozaki, T., Sarai, T., 2016. Implant failure of titanium versus cobalt-chromium growing rods in early-onset scoliosis. *Spine* 41, 502–507. <https://doi.org/10.1097/BRS.0000000000001267>.
- Slivka, M.A., Fan, Y.K., Eck, J.C., 2013. The effect of contouring on fatigue strength of spinal rods: is it okay to re-bend and which materials are best? *Spine Deformity* 1, 395–400. <https://doi.org/10.1016/j.jspd.2013.08.004>.
- Smith, J.S., Shaffrey, C.I., Ames, C.P., Demakakos, J., Fu, K.-M.G., Keshavarzi, S., Li, C.M.Y., Deviren, V., Schwab, F.J., Lafage, V., Bess, S., 2012. Assessment of symptomatic rod fracture after posterior instrumented fusion for adult spinal deformity. *Neurosurgery* 71, 862–867. <https://doi.org/10.1227/NEU.0b013e3182672aab>.
- Stürz, H., Hinterberger, J., Matzen, K., Piltz, W., 1979. Damage analysis of the Harrington rod fracture after scoliosis operation. *Arch. Orthop. Trauma. Surg.* 95, 113–122.
- Suresh, S., 1998. *Fatigue of Materials*. Cambridge university press.
- Teli, M., Grava, G., Solomon, V., Andreoletti, G., Grisoni, E., Meswania, J., 2012. Measurement of forces generated during distraction of growing-rods in early onset scoliosis. *World J. Orthoped.* 3, 15–19. <https://doi.org/10.5312/wjo.v3.i2.15>.
- Teoh, S.H., 2000. Fatigue of biomaterials: a review. *Int. J. Fatig.* 22, 825–837. [https://doi.org/10.1016/S0142-1123\(00\)00052-9](https://doi.org/10.1016/S0142-1123(00)00052-9).
- Thompson, G.H., Akbarnia, B.A., Campbell Jr., R.M., 2007. Growing rod techniques in early-onset scoliosis. *Journal of Pediatric Orthopedics* 27, 354–361. <https://doi.org/10.1097/BPO.0b013e3180333eea>.
- Watanabe, K., Uno, K., Suzuki, T., Kawakami, N., Tsuji, T., Yanagida, H., Ito, M., Hirano, T., Yamazaki, K., Minami, S., Kotani, T., Taneichi, H., Imagama, S., Takeshita, K., Yamamoto, T., Matsumoto, M., 2013. Risk factors for complications associated with growing-rod surgery for early-onset scoliosis. *Spine* 38, E464–E468. <https://doi.org/10.1097/BRS.0b013e318288671a>.
- Waugh, T.R., 1966. Intravital measurements during instrumental correction of idiopathic scoliosis. *Acta Orthop. Scand.* 93, 1–87. <https://doi.org/10.3109/ort.1966.37.suppl-93.01>.
- White, A., Panjabi, M., 1990. *Clinical Biomechanics of the Spine*, second ed. Lippincott Williams & Wilkins, Philadelphia.
- Yamanaka, K., Mori, M., Yamazaki, K., Kumagai, R., Doita, M., Chiba, A., 2015. Analysis of the fracture mechanism of Ti-6Al-4V alloy rods that failed clinically after spinal instrumentation surgery. *Spine* 40, E767–E773. <https://doi.org/10.1097/BRS.0000000000000881>.
- Yang, J.S., Sponseller, P.D., Thompson, G.H., Akbarnia, B.A., Emans, J.B., Yazici, M., Skaggs, D.L., Shah, S.A., Salari, P., Poe-Kochert, C., 2011. Growing rod fractures: risk factors and opportunities for prevention. *Spine* 36, 1639–1644. <https://doi.org/10.1097/BRS.0b013e31822a982f>.
- Yazici, M., Olgun, Z.D., 2013. Growing rod concepts: state of the art. *Eur. Spine J.* 22, 118–130. <https://doi.org/10.1007/s00586-012-2327-7>.
- Yoshihara, H., 2013. Rods in spinal surgery: a review of the literature. *Spine J.* 13, 1350–1358. <https://doi.org/10.1016/j.spinee.2013.04.022>.